

PAPER

[View Article Online](#)
[View Journal](#)

Cite this: DOI: 10.1039/d3ee02129g

Regulating the reorganization energy and crystal packing of small-molecule donors enables the high performance of binary all-small-molecule organic solar cells with a slow film growth rate†

Tongle Xu,^{‡a} Jie Lv,^{‡b} Daming Zheng,^{‡c} Zhenghui Luo,^{id *a} Min Hun Jee,^d Guangliu Ran,^e Zhanxiang Chen,^a Zhongyan Huang,^{id a} Jiaqi Ren,^f Yuxiang Li,^{id f} Cai'e Zhang,^{id a} Hanlin Hu,^{id *b} Thierry Pauporté,^c Wenkai Zhang,^{id *e} Han Young Woo^{id *d} and Chuluo Yang^{id *a}

Difficulty in tuning the ideal phase morphology of interpenetrating network structures is the main reason for the relative inefficiency of all-small-molecule organic solar cells (ASM-OSCs). Achieving a desirable phase morphology is closely tied to both the molecular structure and film-formation process. Therefore, understanding the material's structural properties and film formation mechanism becomes crucial to improve the device performance. Herein, we have developed three small-molecule donors (**T25**, **T26** and **T27**) through stepwise terminal-group and side-chain engineering. For the first time in the ASM-OSCs, we have analyzed the relationship between the material's structure, film formation mechanism and device performance by combining single crystal structure analysis and glow discharge optical emission spectroscopy (GD-OES) measurements. The results demonstrate that **T27** exhibits a lower reorganization energy and a well-connected crystal packing, leading to a higher hole mobility compared to **T25** and **T26**. Device performance results and morphological analysis indicate that the **T27:Y6**-based ASM-OSCs yield enhanced efficiency compared to the **T25**- and **T26**-based ones. This enhancement can be attributed to the better charge generation and transport, suppressed charge recombination, more favorable molecular packing and slower film growth rate. These results not only provide insight into molecular designing, but also contribute to a deeper understanding of the film growth mechanism.

Received 30th June 2023,
Accepted 16th October 2023

DOI: 10.1039/d3ee02129g

rsc.li/ees

Broader context

Bulk heterojunction organic solar cells (OSCs) have gained considerable attention due to their ability to convert optical energy into electricity, offering advantages such as light weight, mechanical flexibility, and semi-transparency. These devices typically consist of a P-type organic semiconductor as the donor and an N-type organic semiconductor as the acceptor. The OSCs can be categorized into two types: polymer OSCs and all-small-molecule OSCs (ASM-OSCs), based on their constituent materials. Recent advancements in device-processing engineering and photovoltaic materials, particularly the development of Y-series acceptors, have led to the ASM-OSCs achieving power conversion efficiencies (PCEs) exceeding 16%. However, the PCEs of the ASM-OSCs still fall behind those of the polymer-based OSCs. One of the key challenges hindering the efficiency of the ASM-OSCs is the achievement of the desired phase morphology of interpenetrating network structures. Therefore, careful consideration and revision of device-processing techniques and the properties of materials are necessary to address this challenge and further enhance the performance of the ASM-OSCs. In this work, we develop three small-molecule donors (**T25**, **T26** and **T27**) by stepwise terminal-group and side-chain engineering. The binary ASM-OSC based on **T27:Y6** yields a high power conversion efficiency (PCE) of 16.8%, significantly higher than those based on **T25:Y6** (12.1%) and **T26:Y6** (14.0%). The better PCE of the **T27:Y6** device reveals a better donor/acceptor molecular aggregation and a slower growth rate of film thickness. Additionally, the **T27:Y6** device yields an impressive PCE of 15.03% with a thickness of 306 nm, indicating that the **T27**-based device exhibits good tolerance to film thickness and is suitable for roll-to-roll fabrication.

^a Shenzhen Key Laboratory of New Information Display and Storage Materials, College of Materials Science and Engineering, Shenzhen University, Shenzhen 518060, China. E-mail: zhhuiluo@szu.edu.cn, clyang@szu.edu.cn

^b Hoffmann Institute of Advanced Materials, Shenzhen Polytechnic, 7098 Liuxian Boulevard, Shenzhen 518055, China. E-mail: hanlinhu@szpt.edu.cn

^c Chimie ParisTech, Université PSL, CNRS, Institut de Recherche de Chimie Paris (IRCP), UMR8247, 11 rue P. et M. Curie, F-75005, Paris, France

^d Department of Chemistry, College of Science, Korea University, Seoul 136-713, Republic of Korea. E-mail: hywoo@korea.ac.kr

^e Department of Physics and Applied Optics Beijing Area Major Laboratory, Beijing Normal University, Beijing 100875, China. E-mail: wkzhang@bnu.edu.cn

^f School of Materials Science and Engineering, Xi'an University of Science and Technology, Xi'an 710054, China

† Electronic supplementary information (ESI) available: Characterization of NMR spectra and MS spectra and additional experimental results. CCDC 2261017 (**T26**) and 2261018 (**T27**). For ESI and crystallographic data in CIF or other electronic format see DOI: <https://doi.org/10.1039/d3ee02129g>

‡ T. Xu, J. Lv and D. Zheng contributed equally to this work.

Introduction

Bulk heterojunction organic solar cells (OSCs) are attracting significant attention due to their ability to convert optical energy into electricity, while being light weight, mechanically flexible, and semi-transparent, among other advantages.^{1–11} Typically, the OSCs are principally composed of a P-type organic semiconductor as the donor and an N-type organic semiconductor as the acceptor. The OSCs can be divided into two categories, polymer OSCs and all-small-molecule OSCs (ASM-OSCs), based on their constituent materials.^{12–19} Compared with the polymer OSCs, the ASM-OSCs have several distinct advantages, including defined chemical structures, easy purification and high batch-to-batch reproducibility of the photovoltaic performance.^{20–25} With recent innovation of device-processing engineering and photovoltaic materials, particularly the development of Y-series acceptors, the power conversion efficiencies (PCEs) of the ASM-OSCs have surpassed 16%.^{26–30} However, the PCEs of the ASM-OSCs still lag behind those of the polymer-based OSCs.^{31,32} Therefore, engineering high-performance small molecule donors (SMDs) is crucial for enhancing the PCEs of the ASM-OSCs.

In A–D–A type SMDs with benzo[1,2-*b*:4,5-*b'*]dithiophene (BDT) as the donor unit, the terminal group plays a crucial role in controlling the absorption, energy level and aggregation propensity, among other factors.^{28,33,34} For instance, Ge's group reported a suite of SMDs using 1*H*-indene-1,3(2*H*)-dione, 2-ethylhexyl rhodanine and cyanoacetic acid esters as terminal groups, respectively. They found that varying the end-group can affect the packing morphology of the active layer, leading to different π – π interactions and distinct photovoltaic performance.³⁵ Side-chain engineering is another frequently used strategy for improving PCE as it can well regulate the surface tension, intermolecular miscibility and charge transport properties.^{22,29,36} Lu and co-workers developed a series of SMDs with siloxane as a side chain, named ZR-SiO and ZR-SiO-EH. Compared with SMD ZR-C8 without siloxane modification, the addition of siloxane to the side chain improved the phase separation, molecular stacking, and bicontinuous nanoscale interpenetrating network, resulting in high PCEs of over 16% for both ZR-SiO and ZR-SiO-EH-based devices.³⁷ Very recently, a report from our group has described two SMDs with different side chains on selenophene conjugated units. The device using T6-based film with trialkylsilyl side chains achieved a remarkable PCE of 16.03%, while the T4-based blend with only alkyl side chains achieved an average PCE of 12.61%, which highlights the significance of side-chain engineering in improving the photovoltaic performance of the ASM-OSCs.²⁷

In addition to the optimization of materials, a thorough understanding of the relationship between the materials' structures and their properties is also important for improving the performance of the OSCs. In previous studies, a class of single crystals of A–D–A type small-molecule acceptors have been analyzed, and the results have confirmed that the single crystal structures have a significant influence on molecular packing, charge transport properties and film morphology.^{38,39} However, for the SMDs, the influence of the donor single crystals on

molecular interaction, morphology and device performance has not been systematically investigated before.^{40,41} Therefore, it is highly essential to study the effect of the single crystal structures on film morphology and device performance. Additionally, the morphology-performance relationship of the OSCs has primarily relied on traditional techniques such as TEM (transmission electron microscopy), GIWAXS (grazing-incidence wide-angle X-ray scattering), and TA (transient absorption spectroscopy), which do not focus on the film-formation process, even though understanding the active layer formation mechanism in the OSCs is crucial for achieving the high PCEs of devices.^{15,42,43}

Herein, three SMDs named **T25**, **T26** and **T27** are designed and developed, all of which employ BDT as the central donor core and phenyl as the conjugated side chain. The main difference between **T25** and **T26** is their terminal groups, with **T25** having cyanoacetic acid esters while **T26** having 2-ethylhexyl rhodanine as its terminal group. **T26** shows redshifted absorption spectra and a deeper HOMO (highest occupied molecular orbital) level in comparison with **T25**. When the fluorine in **T26** is replaced with chlorine to form **T27**, molecular absorption shows a blue shift and the HOMO level shifts downward, consistent with previous reports.⁴⁴ The photovoltaic performance of the ASM-OSC devices using **T25**, **T26**, or **T27** as the donor and **Y6** as the acceptor is systematically optimized, and the results show significant differences. The **T25**-based device attains an unsatisfactory PCE of 12.1%, while the end-group optimized **T26**-based one produces an improved PCE of 14.0%. Furthermore, benefiting from side-chain engineering, the **T27**:**Y6** system acquires the best performance of 16.8%. Remarkably, a high PCE of 15.03% was achieved even when the blend thickness was up to ~ 300 nm. The enhanced performance of the **T27**:**Y6** system could mainly be attributed to the better charge generation and transport, tighter crystal packing and more favorable morphology. Furthermore, we employ the glow discharge optical emission spectroscopy (GD-OES) technique to investigate the film-formation process for the first time. *Ex situ* and *in situ* GD-OES techniques demonstrate that high-efficiency devices exhibit a better donor/acceptor molecular aggregation and the films prepared with slower growth rates display a better morphology and device performance.

Results and discussion

The chemical structures of the three SMDs are displayed in Fig. 1a and the detailed synthetic route is depicted in Scheme S1 (ESI†). The structures of the SMDs are characterized by NMR (nuclear magnetic resonance) and HRMS (high-resolution mass spectrometry). As mentioned above, **T25** and **T26** share the same intermediates but different end groups; they can be easily obtained with high yield through intermediate **2a**. The synthesis method of **T27** is similar to that of **T26**, merely replacing fluorine in substrate **2a** with chlorine. Additionally, the decomposition temperatures (T_d) with 5% weight loss for the three SMDs are above 360 °C, showing a fine thermal stability (Fig. S1, ESI†).

We first compare the molecular energy levels of the three SMDs using density functional theory (DFT) calculations. Table 1 shows that the LUMO (lowest unoccupied molecular orbital) and HOMO (highest occupied molecular orbital) values for the three SMDs are similar. Besides, we calculate the molecular internal reorganization energy (λ_{INT}) of the three SMDs. λ_{INT} can be obtained from the four-point energy equation as below: $\lambda_{\text{INT}} = E_{\text{GC}}^{\text{N}} - E_{\text{GN}}^{\text{N}} + E_{\text{GN}}^{\text{C}} - E_{\text{GC}}^{\text{C}}$, where E^{N} and E^{C} represent the formation energies of the neutral and charged molecules, respectively, and the subscripts GC and GN denote charged and neutral molecular geometries. The computed λ_{INT} s and the four-point energies are presented in Table 1 and Table S1 (ESI[†]), respectively. **T26** and **T27** show a close λ_{INT} of 136 meV, which can be comparable to highly efficient small-molecule acceptors such as **Y6** (137.6 meV) and BTP-PhC6-C11 (136.7 meV).³⁸ In contrast, **T25** with 2-ethylhexyl 2-cyanoacetate as the end group shows a significantly larger λ_{INT} of 154 meV compared to **T26** and **T27**. The low λ_{INT} s are beneficial to their charge mobilities.⁴⁵

To compare the effect of halogens on molecular packing, we perform single crystal diffraction experiments to study the packing behavior of **T26** and **T27**. The single crystals are cultivated in a mixed solution of tetrahydrofuran and isopropanol (1:3 v/v), in which the donor (usually about 1.5 mg) is dissolved in a small amount of tetrahydrofuran followed by adding isopropanol tardily. The resulting mixture forms two phases with isopropanol slowly penetrating into tetrahydrofuran, and eventually the single crystals slowly crystallize out. As shown in Fig. 1b, the two SMDs (**T26**, CCDC: 2261017; **T27**, CCDC: 2261018) show a similar linear molecular geometry and good molecular planarity. It can be found that replacing *F* with *Cl* reduces the S...S distance (from 3.18 Å to 3.16 Å) and the

torsion angle (from 58° to 49°) between the phenyl side chain and BDT, contributing to the connected intermolecular packing. In addition, the two SMDs display obviously different packing motifs. In **T26** single crystals, only a single molecule is involved in a single unit cell, whereas for **T27**, four molecules are involved in a single unit cell (Fig. S2, ESI[†]). The $\pi \cdots \pi$ distances in the dimer are calculated to be 3.60 Å for **T26** and 3.53 Å for **T27** (Fig. 1c). The smaller $\pi \cdots \pi$ distances and torsion angle between the phenyl side chain and BDT in **T27** single crystals are beneficial for improving molecular packing and hole mobility. The hole mobility of the neat film was calculated to be $3.84 \times 10^{-3} \text{ cm}^2 \text{ V}^{-1} \text{ s}^{-1}$ for **T27**, $1.53 \times 10^{-3} \text{ cm}^2 \text{ V}^{-1} \text{ s}^{-1}$ for **T26**, and $1.10 \times 10^{-3} \text{ cm}^2 \text{ V}^{-1} \text{ s}^{-1}$ for **T25** (Fig. S3, ESI[†]), respectively, by employing the space charge-limited current (SCLC) method. The higher hole mobility of **T27** coincides with its tighter crystal packing as compared with **T26**.

UV-vis absorption spectra are applied to investigate the effects of the end-group and side chain engineering on the optical absorption properties of the SMDs. Fig. 2a shows the neat film absorption of the SMDs and **Y6**, while the solution absorption spectra of the SMDs and the D:A blends are presented in Fig. S4 (ESI[†]), and the detailed optical data are outlined in Table 1. In dilute chloroform solution, the three SMDs exhibit similar absorption spectra. Upon going from solutions to films, the three SMDs show varying degrees of redshift due to the strong intermolecular interactions in film states. The strong electron withdrawal of rhodanine and the fluorine atom result in **T26** showing a maximum redshifted absorption, accompanied by a maximum absorption peak (λ_{max}) at 561 nm and an absorption onset (λ_{onset}) at 673 nm as compared with **T25** (λ_{max} = 549 nm; λ_{onset} = 660 nm) and **T27** (λ_{max} = 534 nm; λ_{onset} = 646 nm). The three donors present a

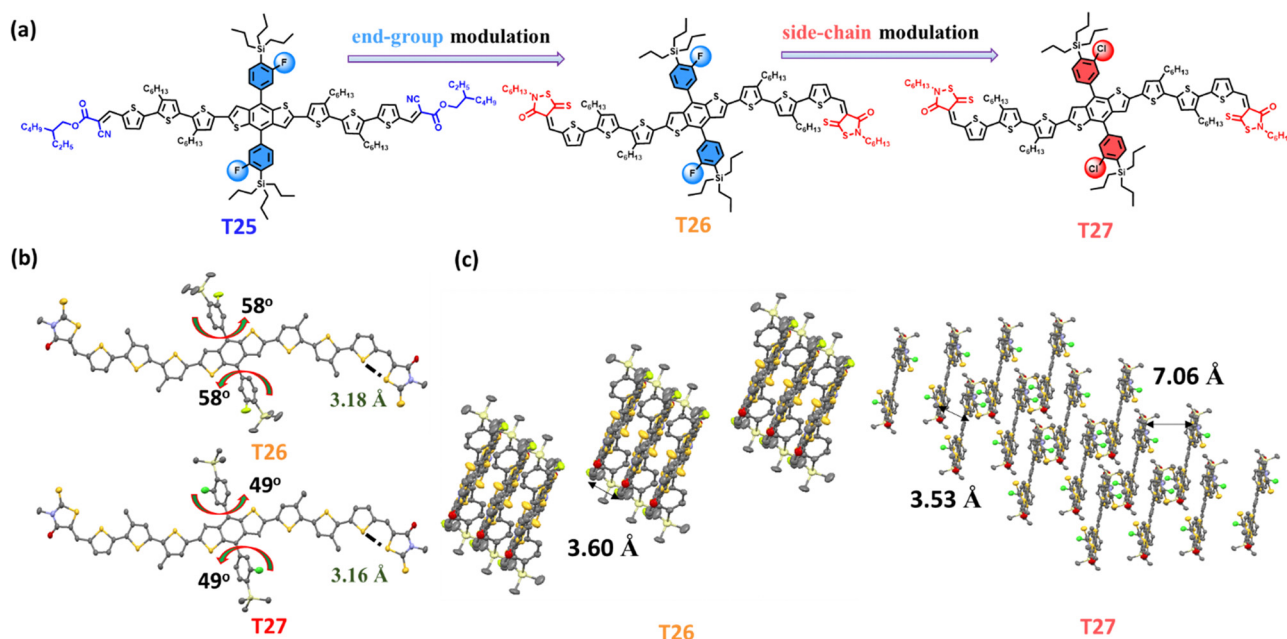


Fig. 1 (a) The chemical structures of **T25**, **T26** and **T27**, and their corresponding electrostatic potentials; (b) the monomolecular single crystallographic structures of **T26** and **T27** in the top-view; and (c) the packing images of **T26** and **T27** single crystals.

Table 1 Physicochemical properties of **T25**, **T26** and **T27**

Donor	$\lambda_{\text{max}}^{\text{sol}}$ (nm)	$\lambda_{\text{max}}^{\text{film}}$ (nm)	$\lambda_{\text{onset}}^{\text{film}}$ (nm)	$E_{\text{g}}^{\text{opt}a}$ (eV)	LUMO ^{CV} (eV)	HOMO ^{CV} (eV)	E_{g}^{CV} (eV)	LUMO ^{DFT} (eV)	HOMO ^{DFT} (eV)	λ_{int} (meV)
T25	502	549	660	1.88	−3.49	−5.36	1.87	−3.03	−5.26	154.4
T26	516	561	673	1.84	−3.67	−5.50	1.83	−3.14	−5.23	136.8
T27	516	534	646	1.91	−3.50	−5.52	2.02	−3.15	−5.24	136.1

^a Calculated from $E_{\text{g}}^{\text{opt}} = 1240/\lambda_{\text{onset}}$.

wide absorption range from 300 to 750 nm, complementing well with a typical narrow band-gap star acceptor **Y6**, which has broad absorption ranging from 600 to 950 nm.³⁰ Electrochemical cyclic voltammetry (CV) is carried out with a ferrocene/ferrocenium (Fc/Fc^+) redox couple as the internal calibration to evaluate the molecular energy levels of the SMDs. As depicted in Fig. 2b and Table 1, the calculated LUMO energy levels are −3.49, −3.67, and −3.50 eV for **T25**, **T26** and **T27**, respectively, and their corresponding HOMO energy levels are −5.36, −5.50 and −5.52 eV, respectively. Notably, the HOMO energy levels of

the SMDs gradually deepen from **T25**, **T26** to **T27**, which may enable the **T27**-based device to hold a higher open-circuit voltage (V_{OC}).⁴⁶

To evaluate the photovoltaic performance of the SMDs, a series of ASM-OSC devices are fabricated with a conventional structure of ITO/PEDOT:PSS (poly(3,4-ethylenedioxythiophene: polystyrenesulfonate)/active layer/PDINN/Ag. Device optimization processes, including the optimization of donor-to-acceptor ratios, post-treatments (such as thermal annealing, solvent vapor annealing or a combination of them), additives, various

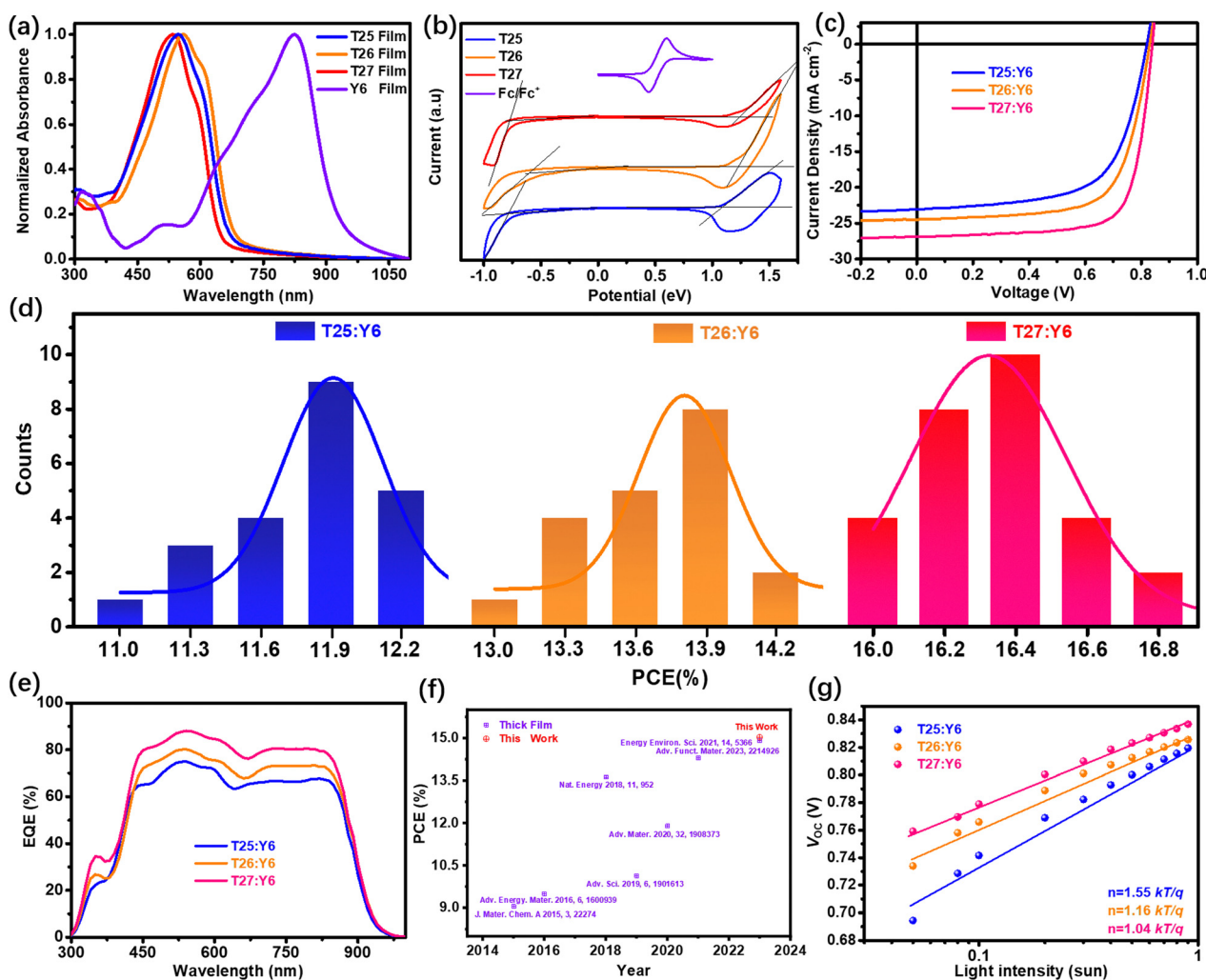


Fig. 2 (a) Normalized absorption spectra of **T25**, **T26**, **T27** and **Y6** in the neat film; (b) cyclic voltammograms of **T25**, **T26**, and **T27**; (c) $J-V$ curves of the best-performing **T25:Y6**, **T26:Y6** and **T27:Y6** devices; (d) the histogram of efficiency distribution of **T25:Y6**, **T26:Y6** and **T27:Y6** devices; (e) EQEs of **T25:Y6**, **T26:Y6** and **T27:Y6** devices; (f) summary of the highest PCEs of the thick-film ASM-OSCs reported in the past 8 years and (g) V_{OC} dependence on the light intensity.

electron transport layers, *etc.*, are carefully conducted, and the detailed optimization processes are summarized in Tables S2–S7 (ESI†). The J - V curves of the optimized devices for the three systems are plotted in Fig. 2c, and the histogram of efficiency distribution and their corresponding photovoltaic parameters are separately summarized in Fig. 2d and Table 2. For the **T25:Y6** based device, a moderate PCE of 12.2% with a corresponding V_{OC} of 0.82 V, a J_{SC} of 23.0 mA cm⁻², and an FF of 64% are obtained. After modifying the terminal group, the performance of the **T26:Y6** based device has been effectively improved, with a recorded PCE of 14.0%. Furthermore, replacing F with Cl endows the **T27:Y6** device with a better PCE of 16.8% for the ASM-OSC devices, accompanied by varying degrees of improvement in V_{OC} , J_{SC} and FF. Although the V_{OC} change is relatively limited, rising from 0.831 to 0.839 V, FF and J_{SC} have significantly enhanced sharply. Specifically, the FF has increased from 68.9% to 74.4%, while J_{SC} has jumped from 24.5 into 26.9 mA cm⁻².

To confirm the J_{SC} values obtained from the J - V curves, the external quantum efficiency (EQE) was measured and is shown in Fig. 2e. The three SDM based devices show a similar photo response range, but with a significantly different response intensity. The EQE of the **T27**-based blend, whose maximum response intensity is around 88%, is distinctly higher than those of the **T25**- and **T26**-based devices, which can clearly explain the corresponding highest J_{SC} among the three systems. The integral J_{SC} values are 21.9, 23.6 and 26.1 mA cm⁻² for **T25**-, **T26**- and **T27**-based devices, respectively, which are in good agreement with the current densities measured from J - V curves with an error of 5%, implying the dependability of the conducted device performance measurements.

The high FF of the **T27**-based device makes it a promising candidate for thick film devices, which are particularly crucial for roll-to-roll printing fabrication. Therefore, we were motivated to further investigate the thickness-dependent ASM-OSC performance by using the **T27 SMD**. As a result, a high PCE of up to 15.03% is obtained for the **T27:Y6** device with the thickness approaching ~300 nm, which is one of the champion values reported for thick film ASM-OSCs (Fig. 2f and Table S8, ESI†).^{25,29} This result indicates that the **T27**-based device exhibits good tolerance to film thickness and is suitable for roll-to-roll fabrication.

To better understand the effects of molecule modification on charge extraction and incident light response, charge carrier dynamics is executed by different means. Firstly, the SCLC method is applied to measure the charge transport properties,⁴⁷ the hole mobility (μ_h) and electron mobility (μ_e) and the

homologous measurement results are presented in Fig. S5 (ESI†). The **T25:Y6** blend shows a μ_h of 0.74×10^{-3} cm² V⁻¹ s⁻¹ and a μ_e of 1.23×10^{-3} cm² V⁻¹ s⁻¹. As the end group changed to rhodanine, the **T26:Y6** blend displays synchronously enhanced μ_h and μ_e of 0.93×10^{-3} and 1.57×10^{-3} cm² V⁻¹ s⁻¹, respectively. Upon further chlorine substitution, the **T27:Y6** system achieves a higher μ_h of 1.28×10^{-3} cm² V⁻¹ and a more balanced ratio (μ_h/μ_e) of 0.94, which can be ascribed to the rod-shaped domain size pattern and an interpenetrating network structure formed in the **T27:Y6** blend (as discussed below). Obviously, the μ_h/μ_e ratio of the **T27**-based device is closer to 1 and those of the **T25**-based device and **T26**-based device are 0.52 and 0.59, respectively, and this should be one of the reasons for the better FF and J_{SC} of the **T27**-based device.⁴⁸

The charge recombination is characterized through the relationship between J_{SC} and P_{light} (light intensity). Generally, it is described by a power law equation: $J_{SC} \propto I^\alpha$, in which α reflects the degree of devices effected by bimolecular recombination.⁴⁹ The α values closer to 1 mean a reduced bimolecular recombination in the bulk. As unveiled in Fig. S6 (ESI†), the α values for **T25**-, **T26**- and **T27**-based devices are fitted to 1.00, 0.99 and 0.99, indicating a negligible bimolecular recombination for the three devices. Furthermore, we investigate the trap-assisted recombination. As shown in Fig. 2g, with the optimization of molecules from the terminal group to side chain, the n values become gradually closer to 1 and decline from 1.54 to 1.09 to 1.02, indicating that the **T25**-based device suffers the most serious trap-assisted recombination among the three systems, while the blend of **T27:Y6** shows the least amount of recombination, which is in line with the reinforced photovoltaic efficiencies.^{50,51} Furthermore, TPV (transient photovoltage) and TPC (transient photocurrent) are determined to gain in-depth insights into the charge recombination and extraction behaviors. TPC measurements primarily reflect the competition between carrier sweep-out and recombination. As fitted in Fig. S7 (ESI†), the photocurrent decay times of the **T25:Y6**, **T26:Y6** and **T27:Y6** blends are found to be 0.335, 0.322 and 0.301 μ s, respectively, demonstrating that the **T27:Y6** system shows a more effective charge carrier extraction than the other two blends.²⁵ On the other hand, TPV measurements are employed to assess carrier lifetimes (τ) under open-circuit conditions, and a longer τ indicates that the devices are less influenced by charge recombination. As shown in Fig. S8 (ESI†), the **T27**-based ASM-OSC discloses the longest τ value of 2.49 μ s in comparison with the **T25**-based (1.03 μ s) and **T26**-based (1.49 μ s) devices, illustrating the suppressed charge recombination in the **T27:Y6** blends. Efficient charge extraction and

Table 2 The photovoltaic data for **T25:Y6**, **T26:Y6** and **T27:Y6** with a ratio of 1.5 : 1. All data were obtained under the illumination of AM 1.5G (100 mW cm⁻²) light source

D : A	V_{OC} (V)	FF (%)	J_{SC} (mA cm ⁻²)	PCE ^a (%)	J_{SC}^b (mA cm ⁻²)
T25:Y6	0.820 (0.817 ± 0.007)	64.0 (62.2 ± 1.9)	23.0 (22.9 ± 0.3)	12.1 (11.7 ± 0.3)	21.9
T26:Y6	0.831 (0.827 ± 0.004)	68.9 (67.2 ± 1.4)	24.5 (24.4 ± 0.1)	14.0 (13.6 ± 0.4)	23.6
T27:Y6	0.839 (0.834 ± 0.009)	74.4 (72.9 ± 0.7)	26.9 (26.7 ± 0.2)	16.8 (16.3 ± 0.2)	26.1

^a Values in parentheses are averages based on 15 independent cells (device area: 0.11 cm²). ^b Integrated J_{SC} from the EQE curves.

reduced charge recombination are helpful for increasing J_{SC} and FF.²⁷ The outcomes further confirm that appropriate molecule designing is proved to be a beneficial approach for facilitating charge carrier extraction and suppressing charge recombination.

The **T27:Y6** device shows a higher J_{SC} , FF and reduced charge recombination in comparison with the **T25-** and **T26-**based films. Generally, these factors are usually caused by the morphology of the active layer, which is mainly determined by their molecular structures. To preliminary explore the phase separation of the morphology, AFM and TEM measurements are executed on the optimal **T25:Y6**, **T26:Y6** and **T27:Y6** blend films. As depicted in Fig. 3a, the root mean square (RMS) roughness value of **T27:Y6** is 1.96 nm, slightly larger than those of **T25-** (1.92 nm) and **T26-**based devices (1.54 nm), implying enhanced molecular aggregation with excellent crystallinity in the **T27:Y6** device.⁵² Fig. 3b demonstrates the TEM images of the optimal devices. Rod-like patterns with a

well-mixed interpenetrating network structure can be obviously distributed in the whole bulk of the **T27**-based device, which is expected to boost exciton extraction and carrier charge transport, thereby benefiting the device performance.^{53,54}

GIWAXS is likewise adopted to better gain insight into the influence of molecular optimization on molecular packing and crystallinity.⁵⁵ Fig. 3c–g illustrate the 2D GIWAXS patterns and the corresponding 1D line cutting profiles of the pristine and blend films. The detailed GIWAXS parameters are summarized in Tables S9 and S10 (ESI†). The neat films of **T25**, **T26** and **T27** show a similar molecular packing and orientation, in the in-plane (IP) direction, and the three SMDs exhibit prominent edge-on oriented (010) π - π stacking peaks and distinctly multiple ($h00$) lamellar peaks. The d -spacing of (010) π - π stacking in the IP direction for **T27** is 3.5 \AA^{-1} , smaller than that for **T26** (3.7 \AA^{-1}) and **T25** (3.6 \AA^{-1}), indicating a tighter π - π stacking in the neat film of **T27**, which is in accordance with the tendency observed for the single crystals. Similar data can also

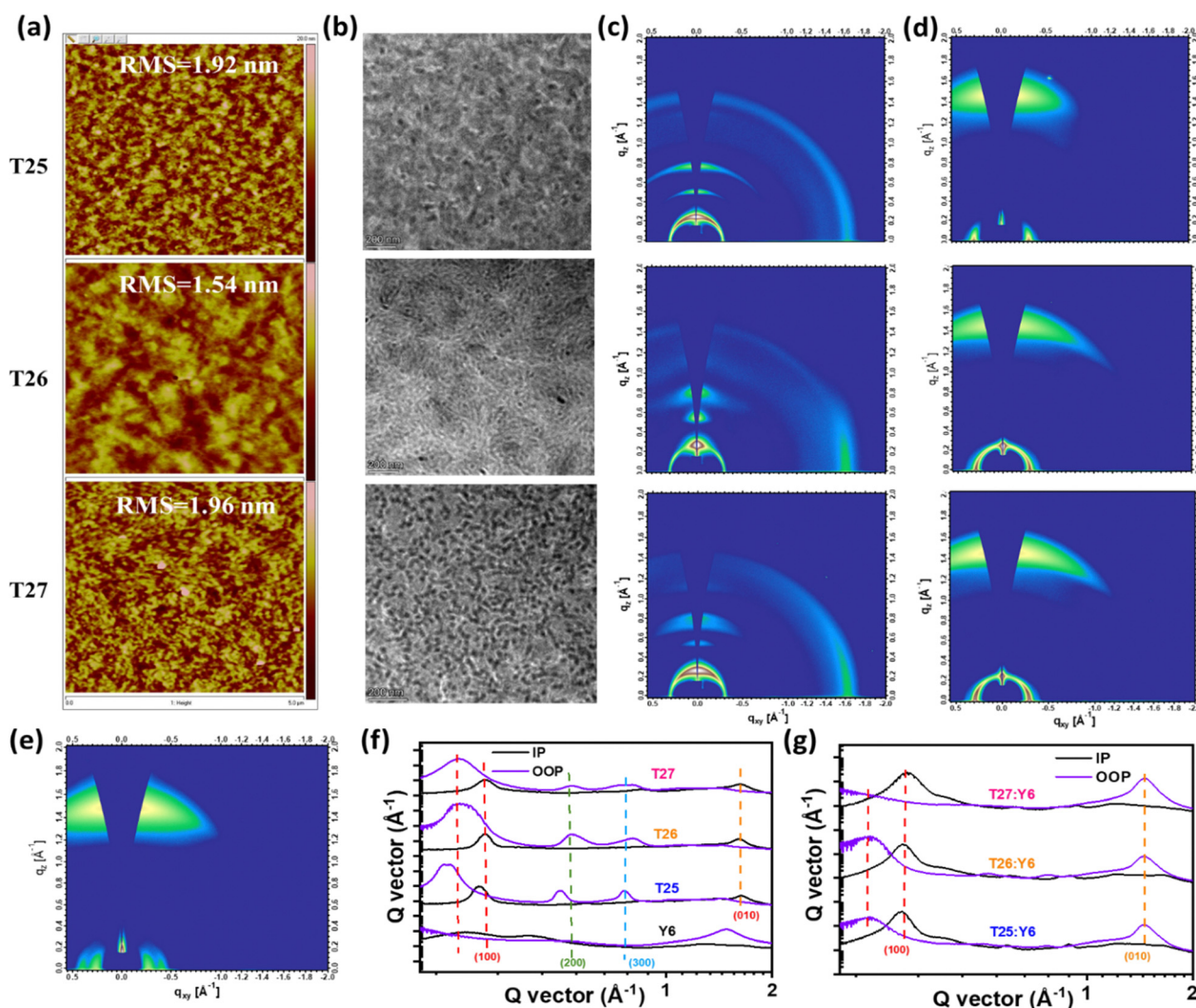


Fig. 3 (a) AFM and (b) TEM images of **T25:Y6**, **T26:Y6** and **T27:Y6** blend films; 2D GIWAXS diffraction patterns of (c) neat **T25**, **T26** and **T27** films and (d) **T25:Y6**, **T26:Y6** and **T27:Y6** blend films; (e) 2D GIWAXS diffraction patterns of **Y6**; the corresponding in-plane (IP) and out-of-plane (OOP) line-cut profiles of (f) neat films and (g) blend films.

be found for (*h*00) π - π stacking in the IP direction. In the out-of-plane (OOP) direction, the donors perform contradictory molecular packing, strong multiple (*h*00) lamellar peaks can easily be observed, and the face-on oriented (010) π - π stacking peak is imperceptible, except that SMD T25 shows a faint π - π stacking peak with q_z at 1.527 \AA^{-1} . Upon blending with Y6, a high crystallinity star acceptor with dominant face-on orientation, the molecular packing features and crystallinity behaviors of the blends are significantly unique. All optimal blends show a remarkable face-on orientation with obvious π - π molecular packing in the OOP direction instead of the edge-on orientation of the neat films in the IP direction. The T27-based device exhibits a bright (010) π - π stacking distance (d_{spacing}) of 3.7 \AA with q_z at 1.697 \AA^{-1} , along with a crystal coherence length (CCL) of 32.9 \AA in the OOP direction. The T27:Y6 film displays a higher CCL value and a low d_{spacing} value compared to the T26- and T25-based devices, whose CCL values are 28.1 and 30.0 \AA , respectively, with a d_{spacing} of 3.8 \AA with q_z at 1.633 \AA^{-1} , revealing that the T27:Y6 film presents a

higher crystallinity and more obvious face-on π - π stacking properties than the other two blends. The enhanced CCL and smaller d_{spacing} can virtually benefit intermolecular charge transport and prolong the charge carrier lifetime, thus finally resulting in the enhanced device performance.^{56,57}

We investigate the exciton generation and diffusion processes of the three devices using femtosecond transient absorption (fs-TA) spectroscopy. Fig. 4a–c display the contour plots of the time-resolved absorption difference spectra of T25:Y6, T26:Y6, and T27:Y6 blend films pumped at 800 nm . From the fs-TA spectra at different time delays in Fig. 4b–f, we observe a strong ground-state bleach (GSB) signal in the acceptor absorption wavelength range immediately following excitation in the three blends, indicating the formation of excitons in the acceptor domain. Since the donor molecules are almost not absorbed at 800 nm , only the acceptor molecules can be excited at 800 nm . However, we still observed a slowly increasing negative signal with time delay in the range of 550 – 675 nm (corresponding to the donor absorption range)

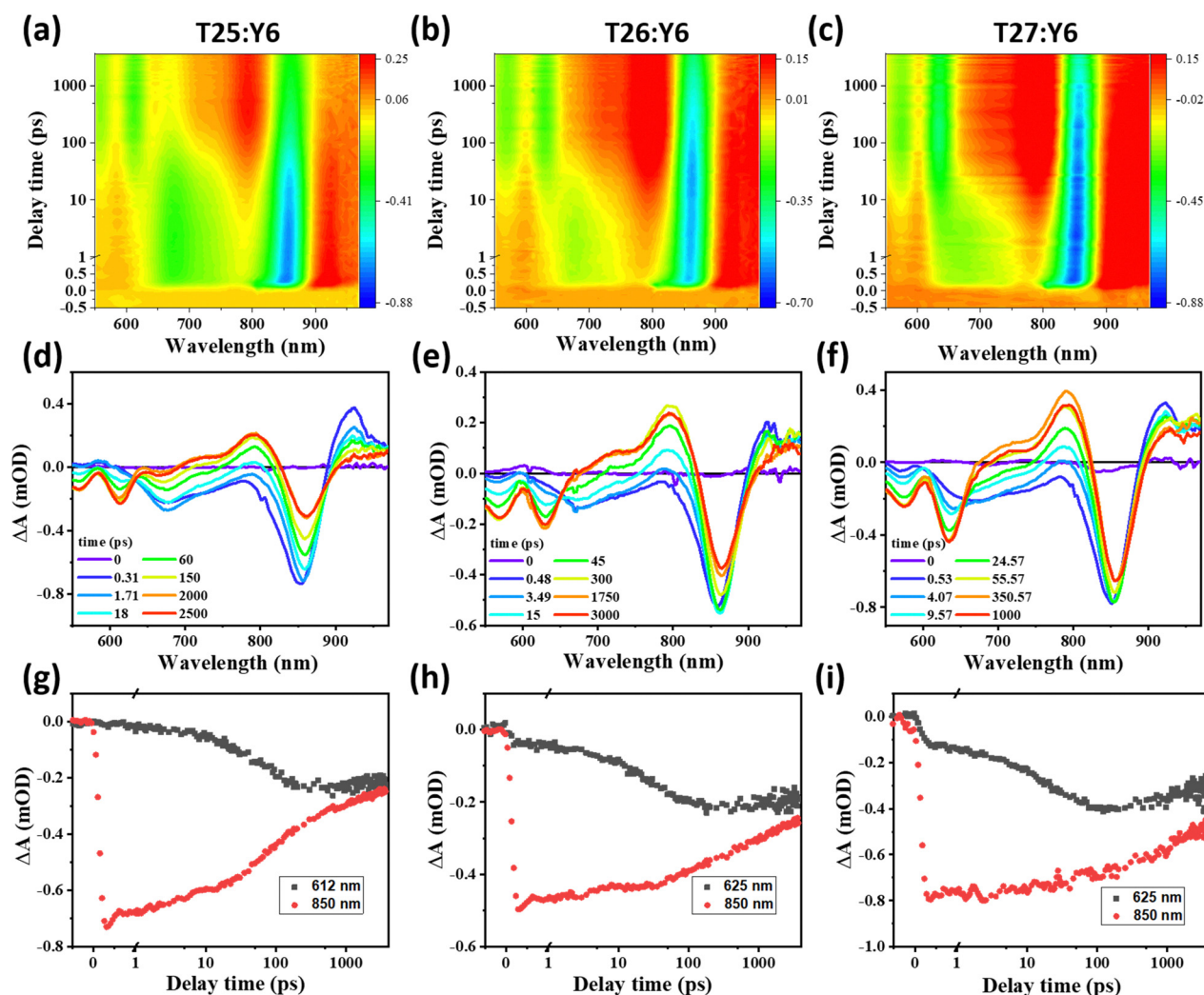


Fig. 4 (a)–(c) Contour plots of the time-resolved absorption difference spectra of T25:Y6, T26:Y6 and T27:Y6 blend films; (d)–(f) fs-TA spectra at different time delays of T25:Y6, T26:Y6 and T27:Y6 blend films; and (g)–(i) GSB decay signal of T25:Y6, T26:Y6 and T27:Y6 blend films.

due to the efficient hole transfer process in the bulk-heterojunction.^{58,59}

The GSB signal of each blend is shown in Fig. 4g–i, where the signal change is more pronounced. By fitting the GSB signal of the donor with a multi-exponential function, we determined the time constants of the blend films as below: **T25:Y6** ($\tau_1 = 0.99 \pm 0.30$ ps, $\tau_2 = 74.39 \pm 5.84$ ps), **T26:Y6** ($\tau_1 = 0.56 \pm 0.12$ ps, $\tau_2 = 31.73 \pm 1.26$ ps), and **T27:Y6** ($\tau_1 = 0.22 \pm 0.02$ ps, $\tau_2 = 20.61 \pm 0.56$ ps), where τ_1 and τ_2 are assigned as the ultrafast exciton dissociation at the interface and the diffusion of the exciton in the domain.⁶⁰ The **T27:Y6** system exhibits the fastest exciton dissociation and diffusion, which is beneficial for charge generation and consistent with the superior performance of the corresponding devices.

To gain a more intuitive and deeper understanding of donor-acceptor molecular aggregation and longitudinal distribution within the three films, we conduct glow discharge optical emission spectroscopy (GD-OES) experiments on the active layer preparation.^{61–64} Our study is the first to employ the *in situ/ex situ* GD-OES technique to provide the depth profiles of the main elements in the active layers of the OSCs. We achieve this by sputtering the complete active layer directly with Ar and detecting the optical emission of the elements released from it. This method allows us to obtain the depth profile distribution of the elements comprising the active layer. The functioning of GD-OES equipment is illustrated in Fig. S1a (ESI[†]). The sputtering plasma and probed sample surface were delimited by an O-ring of 4 mm diameter, reflecting the overall situation of the active layer, as shown in Fig. 4a. We begin by measuring the

compositional profile of the full layers by using *ex situ* GD-OES and investigating the molecular aggregation degree of donor-acceptor on these profiles (Fig. 5a and Fig. S9, ESI[†]). We focus on two main organic elements of the structure, namely C and S. Carbon is chosen for two reasons: (1) carbon is the main component of the acceptor, not only in the system studied in this work, but also in any other donor-acceptor system, making it universally detectable and (2) the carbon content does not differ significantly between the donor and acceptor, allowing us to assess the molecular aggregation conditions of both the donor and acceptor based on the distribution of carbon. We have calculated the concentration of carbon and sulfur, and the corresponding average values based on at least five independent experiments are summarized in Table S11 (ESI[†]). The higher carbon concentration in the acceptor and donor indicates that carbon can serve an element to measure the degree of donor/acceptor binding.

Through detection of the longitudinal distribution of sulfur in the thin film, we are able to analyze the specific range of the donor and the diffusivity of the donor in more detail. Analysis of Fig. 5b–d revealed that the distribution of carbon elements in **T27:Y6** (Fig. 4b) is more uniform compared to that in **T26:Y6** (Fig. 5c) and **T25:Y6** (Fig. 5b), indicating a better combination of the donor and acceptor. By analyzing the distribution of carbon, we can assess the binding conditions between the donor and acceptor. In other words, it indicates a better molecular aggregation of the donor and acceptor throughout the film. Conversely, if the distribution curve of carbon elements shows a polarized distribution, with carbon concentrated in the

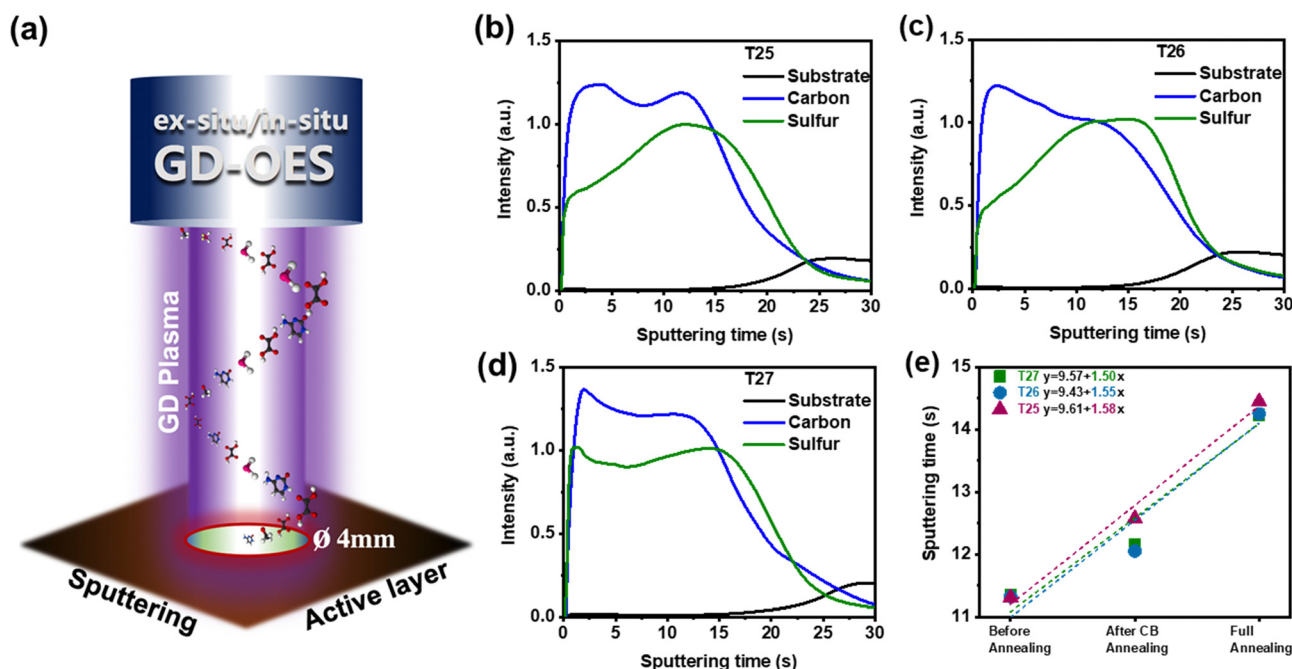


Fig. 5 (a) Investigated solar cells' architecture with the scale of the GD plasma beam passing through the organic layer (the detection diameter is 4 mm). (b)–(d) The GD-OES depth profiles of the fully annealed organic layers of (b) **T25:Y6**, (c) **T26:Y6**, and (d) **T27:Y6**. (e) The GD-OES profiles of the thickness of the organic layer at different annealing stages and the corresponding fitting lines (green dashed line: linear fitting line of **T27:Y6**; blue dashed line: linear fitting line of **T26:Y6**; purple dashed line: linear fitting line of **T25:Y6**).

upper and lower layers of the film, then the combination between the donor and acceptor is poor, just like the results for the **T25:Y6** system in the main paper. In addition, we detect the distribution of chlorine and fluorine in the **T27:Y6** system to determine the distribution of donors and acceptors (Fig. S9b, ESI[†]), as chlorine is only present in **T27** and fluorine is only present in **T26**, and their distribution in the film confirms the conclusion drawn from the carbon curves. Moreover, the main peaks of these two elements in Fig. S9b (ESI[†]) show a complementary distribution, further confirming the distribution of donors and acceptors throughout the active layer, where the donors are mainly distributed in the upper layer and the acceptors are mainly distributed in the lower layer.

The sulfur element curve revealed a polarized distribution of the **T25:Y6** and **T26:Y6** blends, indicating a poor reactive molecular aggregation in these films. This result is consistent with the above GIWAXS and TEM results. In the second step, we perform the GD-OES tracking of the substrate peak at each stage of post-processing in real time (Fig. S9c–e, ESI[†]) and plotted it in Fig. 5e. We determined the slope of the linear fits for the different active layers and defined the value of the slope in terms of the relative growth rate of each active layer. By analyzing and comparing the slopes of the three curves (Fig. 5e), we are able to clearly assess the growth ratio of the films for the different active layers. Among them, the **T27:Y6** blend exhibits a smaller film growth ratio of 1.50 than **T25:Y6** (1.58) and **T26:Y6** (1.55). This indicates that during the post-processing of the active layer, there is a better and stronger agglomeration of the donor and acceptor at a relatively slow rate. In conjunction with the previous GIWAXS results, we know that slower film growth leads to a more ordered and tighter molecular packing, which results in the enhanced FF and J_{sc} of the **T27:Y6** device.

Conclusion

To sum up, we have designed and synthesized three A–D–A type SMDs (**T25**, **T26** and **T27**) using a carefully tailored approach involving terminal-group engineering and side-chain engineering. DFT calculations have shown that using 2-ethylhexyl rhodanine as the end group instead of cyanoacetic acid esters can significantly reduce the internal reorganization energy. Single crystal analysis has revealed that replacing F with Cl endows **T27** with a tighter crystal packing and a smaller S···S distance compared to **T26**. As a result, the **T27**-based binary device displays an outstanding PCE of 16.8%, surpassing the PCEs of **T25**-based (12.1%) and **T26**-based (14.0%) blends. The brilliant performance can be mainly contributed by the higher and balanced charge mobility, suppressed charge recombination, improved charge generation, and a more pronounced fibrous interpenetrating network with tighter π – π stacking. Further investigations using *in situ* and *ex situ* GD-OES indicate that the growth rate of film thickness is consciously related to film morphology and device efficiency. The **T27**-based blend exhibits the slowest film growth rate, resulting in a more

ordered and tightly packed molecular structure, as confirmed by GIWAXS results. Furthermore, the **T27:Y6** device achieves an impressive PCE of 15.03% with the thickness approaching ~300 nm, representing one of the champion values for thick film ASM-OSCs. Our study demonstrates that the development of SMDs with low reorganization energy and compact crystal packing is beneficial for realizing highly efficient ASM-OSCs. Additionally, we found that slow film growth rates are favorable for achieving ordered molecular packing and superior crystal-line properties, which are crucial for the device performance.

Author contributions

T. Xu and Z. Luo conceived the idea. T. Xu synthesized the new donors of **T25**, **T26** and **T27**. J. Lv performed device fabrication and optimization. H. Hu provided the device platform and acceptor materials. C. Yang provided the synthetic platform. C. Zhang completed AFM and TEM experiments. M. H. Jee, J. Re, Y. Li and H. Y. Woo carried out 2D GIWAXS measurements and analysis. Z. Chen conducted DFT calculations. G. Ran and W. Zhang performed TA experiments and analysis. D. Zheng and T. Pauporté performed GD-OES experiments and analysis. Z. Huang completed the single crystal growth. T. Xu and Z. Luo wrote the original manuscript. All authors discussed the results and revised the manuscript. Z. Luo and C. Yang supervised the project.

Conflicts of interest

There are no conflicts to declare.

Acknowledgements

The work described in this paper was supported by the Shenzhen Science and Technology Program (RCBS20221008093225021 and ZDSYS20210623091813040) and the National Natural Science Foundation of China (NSFC, no. 22309119). Y. Li is thankful for the support from the Science and Technology Program of Shanxi Province (2022JM-229). We appreciate for the help received from Professor Zhipeng Kan (Guangxi University), Professor Shirong Lu (Taizhou University) and Professor Guangye Zhang (Shenzhen Technology University). We also thank the Instrumental Analysis Center of Shenzhen University for the Analytical Support.

References

- 1 T. Liu, K. Zhou, R. Ma, L. Zhang, C. Huang, Z. Luo, H. Zhu, S. Yao, C. Yang, B. Zou and L. Ye, *Aggregate*, 2022, **4**, e308, DOI: [10.1002/agt2.308](https://doi.org/10.1002/agt2.308).
- 2 Z. Luo, R. Ma, J. Yu, H. Liu, T. Liu, F. Ni, J. Hu, Y. Zou, A. Zeng, C. J. Su, U. S. Jeng, X. Lu, F. Gao, C. Yang and H. Yan, *Natl. Sci. Rev.*, 2022, **9**, nwac076.

- 3 J. Lv, H. Tang, J. Huang, C. Yan, K. Liu, Q. Yang, D. Hu, R. Singh, J. Lee, S. Lu, G. Li and Z. Kan, *Energy Environ. Sci.*, 2021, **14**, 3044–3052.
- 4 W. Zou, C. Han, X. Zhang, J. Qiao, J. Yu, H. Xu, H. Gao, Y. Sun, Y. Kan, X. Hao, G. Lu, Y. Yang and K. Gao, *Adv. Energy Mater.*, 2023, **13**, 2300784, DOI: [10.1002/aenm.202300784](https://doi.org/10.1002/aenm.202300784).
- 5 P. Cheng, G. Li, X. W. Zhan and Y. Yang, *Nat. Photon.*, 2018, **12**, 131–142.
- 6 T. Xu, Z. Luo, R. Ma, Z. Chen, T. A. Dela Pena, H. Liu, Q. Wei, M. Li, C. Zhang, J. Wu, X. Lu, G. Li and C. Yang, *Angew. Chem., Int. Ed.*, 2023, **63**, e202304127.
- 7 Q. Bai, Q. Liang, H. Li, H. Sun, X. Guo and L. Niu, *Aggregate*, 2022, **3**, e281.
- 8 B. Fan, F. Lin, X. Wu, Z. Zhu and A. K. Jen, *Acc. Chem. Res.*, 2021, **54**, 3906–3916.
- 9 C. Yan, J. Qin, Y. Wang, G. Li and P. Cheng, *Adv. Energy Mater.*, 2022, **12**, 2201087.
- 10 H. Qin, S. Ju, W. Su, B. Zhao, Q. Fan, Z. Bi, S. Zhang, J. Yu, G. Lu, J.-T. Hou, W. Ma, C. Gao and Y. Li, *J. Mater. Chem. C*, 2023, **11**, 750–758.
- 11 W. Xu, D. Wang and B. Z. Tang, *Angew. Chem., Int. Ed.*, 2021, **60**, 7476–7487.
- 12 H. Chen, H. Liang, Z. Guo, Y. Zhu, Z. Zhang, Z. Li, X. Cao, H. Wang, W. Feng, Y. Zou, L. Meng, X. Xu, B. Kan, C. Li, Z. Yao, X. Wan, Z. Ma and Y. Chen, *Angew. Chem., Int. Ed.*, 2022, **61**, e202209580.
- 13 Z. J. Li, X. P. Xu, G. J. Zhang, T. Yu, Y. Li and Q. Peng, *Solar RRL*, 2018, **2**, 1800186.
- 14 C. Li, J. Zhou, J. Song, J. Xu, H. Zhang, X. Zhang, J. Guo, L. Zhu, D. Wei, G. Han, J. Min, Y. Zhang, Z. Xie, Y. Yi, H. Yan, F. Gao, F. Liu and Y. Sun, *Nat. Energy*, 2021, **6**, 605–613.
- 15 J. Ge, L. Xie, R. Peng and Z. Ge, *Adv. Mater.*, 2023, **35**, 2206566.
- 16 J. Wang and X. Zhan, *Acc. Chem. Res.*, 2021, **54**, 132–143.
- 17 R. Ma, X. Jiang, J. Fu, T. Zhu, C. Yan, K. Wu, P. Müller-Buschbaum and G. Li, *Energy & Environ. Sci.*, 2023, **16**, 2316–2326, DOI: [10.1039/d3ee00294b](https://doi.org/10.1039/d3ee00294b).
- 18 Z. Luo, T. Xu, C. E. Zhang and C. Yang, *Energy Environ. Sci.*, 2023, **16**, 2732–2758, DOI: [10.1039/d3ee00908d](https://doi.org/10.1039/d3ee00908d).
- 19 H. Qin, S. Xia, D. Sun, Z. Wu, Y. Wang, Y. Ran, G. Lu, H. Y. Woo, B. Zhao, C. Gao and Y. Li, *J. Mater. Chem. C*, 2022, **10**, 16397–16406.
- 20 J. Qin, C. An, J. Zhang, K. Ma, Y. Yang, T. Zhang, S. Li, K. Xian, Y. Cui, Y. Tang, W. Ma, H. Yao, S. Zhang, B. Xu, C. He and J. Hou, *Sci. Chin. Mater.*, 2020, **63**, 1142–1150.
- 21 J. Guo, B. Qiu, D. Yang, C. Zhu, L. Zhou, C. Su, U. S. Jeng, X. Xia, X. Lu, L. Meng, Z. Zhang and Y. Li, *Adv. Funct. Mater.*, 2021, **32**, 2110159.
- 22 L. Zhang, X. Zhu, D. Deng, Z. Wang, Z. Zhang, Y. Li, J. Zhang, K. Lv, L. Liu, X. Zhang, H. Zhou, H. Ade and Z. Wei, *Adv. Mater.*, 2022, **34**, e2106316.
- 23 Z. Li, X. Wang, N. Zheng, A. Saparbaev, J. Zhang, C. Xiao, S. Lei, X. Zheng, M. Zhang, Y. Li, B. Xiao and R. Yang, *Energy Environ. Sci.*, 2022, **15**, 4338–4348.
- 24 X. Wang, Z. Li, X. Zheng, C. Xiao, T. Hu, Y. Liao and R. Yang, *Adv. Funct. Mater.*, 2023, **33**, 2300323, DOI: [10.1002/adfm.202300323](https://doi.org/10.1002/adfm.202300323).
- 25 T. Xu, J. Lv, K. Yang, Y. He, Q. Yang, H. Chen, Q. Chen, Z. Liao, Z. Kan, T. Duan, K. Sun, J. Ouyang and S. Lu, *Energy Environ. Sci.*, 2021, **14**, 5366–5376.
- 26 Y. Sun, L. Nian, Y. Kan, Y. Ren, Z. Chen, L. Zhu, M. Zhang, H. Yin, H. Xu, J. Li, X. Hao, F. Liu, K. Gao and Y. Li, *Joule*, 2022, **6**, 1–14.
- 27 T. Xu, J. Lv, Z. X. Chen, Z. H. Luo, G. Y. Zhang, H. Liu, H. Huang, D. Q. Hu, X. H. Lu, S. R. Lu and C. L. Yang, *Adv. Funct. Mater.*, 2022, **33**, 2210549.
- 28 H. F. Zhi, M. Jiang, H. Zhang, Q. An, H. R. Bai, M. H. Jee, H. Y. Woo, D. Li, X. Huang and J. L. Wang, *Adv. Funct. Mater.*, 2023, **33**, 2300878, DOI: [10.1002/adfm.202300878](https://doi.org/10.1002/adfm.202300878).
- 29 K. Ma, W. Feng, H. Liang, H. Chen, Y. Wang, X. Wan, Z. Yao, C. Li, B. Kan and Y. Chen, *Adv. Funct. Mater.*, 2023, **33**, 2214926, DOI: [10.1002/adfm.202214926](https://doi.org/10.1002/adfm.202214926).
- 30 J. Yuan, Y. Zhang, L. Zhou, G. Zhang, H.-L. Yip, T.-K. Lau, X. Lu, C. Zhu, H. Peng, P. A. Johnson, M. Leclerc, Y. Cao, J. Ulanski, Y. Li and Y. Zou, *Joule*, 2019, **3**, 1140–1151.
- 31 L. Zhu, M. Zhang, J. Xu, C. Li, J. Yan, G. Zhou, W. Zhong, T. Hao, J. Song, X. Xue, Z. Zhou, R. Zeng, H. Zhu, C. C. Chen, R. C. I. MacKenzie, Y. Zou, J. Nelson, Y. Zhang, Y. Sun and F. Liu, *Nat. Mater.*, 2022, **21**, 656–663.
- 32 W. Gao, F. Qi, Z. Peng, F. R. Lin, K. Jiang, C. Zhong, W. Kaminsky, Z. Guan, C. S. Lee, T. J. Marks, H. Ade and A. K. Jen, *Adv. Mater.*, 2022, **34**, e2202089.
- 33 H. Bin, J. Yao, Y. Yang, I. Angunawela, C. Sun, L. Gao, L. Ye, B. Qiu, L. Xue, C. Zhu, C. Yang, Z. G. Zhang, H. Ade and Y. Li, *Adv. Mater.*, 2018, **30**, e1706361.
- 34 L. L. Zhang, R. Sun, Z. Q. Zhang, J. Q. Zhang, Q. L. Zhu, W. Ma, J. Min, Z. X. Wei and D. Deng, *Adv. Mater.*, 2022, **34**, e2207020.
- 35 J. Ge, L. Hong, H. Ma, Q. Ye, Y. Chen, L. Xie, W. Song, D. Li, Z. Chen, K. Yu, J. Zhang, Z. Wei, F. Huang and Z. Ge, *Adv. Mater.*, 2022, **34**, e2202752.
- 36 J. Ge, L. Xie, R. Peng, B. Fanady, J. Huang, W. Song, T. Yan, W. Zhang and Z. Ge, *Angew. Chem., Int. Ed.*, 2020, **59**, 2808–2815.
- 37 Y. L. Chang, X. W. Zhu, Y. A. Shi, Y. A. Liu, K. Meng, Y. X. Li, J. W. Xue, L. Y. Zhu, J. Q. Zhang, H. Q. Zhou, W. Ma, Z. X. Wei and K. Lu, *Energy Environ. Sci.*, 2022, **15**, 2937–2947.
- 38 Z. Luo, Y. Gao, H. Lai, Y. Li, Z. Wu, Z. Chen, R. Sun, J. Ren, C. E. Zhang, F. He, H. Woo, J. Min and C. Yang, *Energy Environ. Sci.*, 2022, **15**, 4601–4611.
- 39 C. Yang, Q. An, H. R. Bai, H. F. Zhi, H. S. Ryu, A. Mahmood, X. Zhao, S. Zhang, H. Y. Woo and J. L. Wang, *Angew. Chem., Int. Ed.*, 2021, **60**, 19241–19252.
- 40 K. Sun, Z. Xiao, S. Lu, W. Zajackowski, W. Pisula, E. Hanssen, J. M. White, R. M. Williamson, J. Subbiah, J. Ouyang, A. B. Holmes, W. W. Wong and D. J. Jones, *Nat. Commun.*, 2015, **6**, 6013.
- 41 R. Zhou, Z. Jiang, C. Yang, J. Yu, J. Feng, M. A. Adil, D. Deng, W. Zou, J. Zhang, K. Lu, W. Ma, F. Gao and Z. Wei, *Nat. Commun.*, 2019, **10**, 5393.

- 42 H. Gao, Y. Sun, L. Meng, C. Han, X. Wan and Y. Chen, *Small*, 2022, **19**, e2205594.
- 43 B. Kan, Y. Y. Kan, L. J. Zuo, X. L. Shi and K. Gao, *InfoMat*, 2021, **3**, 175–200.
- 44 Z. K. Ji, X. P. Xu, G. J. Zhang, Y. Li and Q. Peng, *Nano Energy*, 2017, **40**, 214–223.
- 45 S. M. Swick, J. M. Alzola, V. K. Sangwan, S. H. Amsterdam, W. Zhu, L. O. Jones, N. Powers-Riggs, A. Facchetti, K. L. Kohlstedt, G. C. Schatz, M. C. Hersam, M. R. Wasielewski and T. J. Marks, *Adv. Energy Mater.*, 2020, **10**, 2000635.
- 46 T. L. Xu, Y. Y. Chang, C. Q. Yan, Q. G. Yang, Z. P. Kan, R. Singh, M. Kumar, G. Li, S. R. Lu and T. N. Duan, *Sustainable Energy Fuels*, 2020, **4**, 2680–2685.
- 47 Y. Shen, A. R. Hosseini, M. H. Wong and G. G. Malliaras, *Chem. Phys. Chem.*, 2004, **5**, 16–25.
- 48 L. K. Huang and Z. Y. Ge, *Adv. Energy Mater.*, 2019, **9**, 1900248.
- 49 P. Schilinsky, C. Waldauf and C. J. Brabec, *Appl. Phys. Lett.*, 2002, **81**, 3885–3887.
- 50 X. Dong, K. Yang, H. Tang, D. Hu, S. Chen, J. Zhang, Z. Kan, T. Duan, C. Hu, X. Dai, Z. Xiao, K. Sun and S. Lu, *Solar RRL*, 2019, **4**, 1900326.
- 51 J. Lv, Q. Yang, W. Deng, H. Chen, M. Kumar, F. Zhao, S. Lu, H. Hu and Z. Kan, *Chem. Eng. J.*, 2023, **465**, 142822.
- 52 W. Su, Y. Wang, Z. Yin, Q. Fan, X. Guo, L. Yu, Y. Li, L. Hou, M. Zhang, Q. Peng, Y. Li and E. Wang, *ChemSusChem*, 2021, **14**, 3535–3543.
- 53 F. G. Guijarro, R. Caballero, P. de la Cruz, R. Singhal, F. Langa and G. D. Sharma, *Solar RRL*, 2020, **4**, 2000460.
- 54 B. Liu, H. Sun, J. W. Lee, Z. Jiang, J. Qiao, J. Wang, J. Yang, K. Feng, Q. Liao, M. An, B. Li, D. Han, B. Xu, H. Lian, L. Niu, B. J. Kim and X. Guo, *Nat. Commun.*, 2023, **14**, 967.
- 55 J. Rivnay, S. C. Mannsfeld, C. E. Miller, A. Salleo and M. F. Toney, *Chem. Rev.*, 2012, **112**, 5488–5519.
- 56 H. Hu, L. Ye, M. Ghasemi, N. Balar, J. J. Rech, S. J. Stuard, W. You, B. T. O'Connor and H. Ade, *Adv. Mater.*, 2019, **31**, e1808279.
- 57 C. He, Y. Pan, Y. Ouyang, Q. Shen, Y. Gao, K. Yan, J. Fang, Y. Chen, C.-Q. Ma, J. Min, C. Zhang, L. Zuo and H. Chen, *Energy Environ. Sci.*, 2022, **15**, 2537–2544.
- 58 J. Zeb, G. Ran, X. Wang, H. Lu, Y. Liu, Z. Bo and W. Zhang, *J. Phys. Chem. C*, 2021, **125**, 23613–23621.
- 59 G. Ran, J. Zeb, H. Lu, Y. Liu, A. Zhang, L. Wang, Z. Bo and W. Zhang, *J. Phys. Chem. Lett.*, 2022, **13**, 5860–5866.
- 60 Z. Chen, X. Chen, B. Qiu, G. Zhou, Z. Jia, W. Tao, Y. Li, Y. M. Yang and H. Zhu, *J. Phys. Chem. Lett.*, 2020, **11**, 3226–3233.
- 61 D. Zheng, F. Raffin, P. Volovitch and T. Pauporte, *Nat. Commun.*, 2022, **13**, 6655.
- 62 D. Zheng, C. Schwob, Y. Prado, Z. Ouzit, L. Coolen and T. Pauporté, *Nano Energy*, 2022, **94**, 106934.
- 63 D. Zheng, T. Zhu, Y. Yan and T. Pauporté, *Adv. Energy Mater.*, 2022, **12**, 2103618.
- 64 D. Zheng, P. Volovitch and T. Pauporte, *Small Methods*, 2022, **6**, e2200633.